Theor Chem Acc (2010) 127:507–517
DOI 10.1007/s00214-010-0739-1

REGULAR ARTICLE

Theoretical study of spin–orbit coupling and kinetics in spin-forbidden reaction between $Ta(NH_2)_3$ and N_2O

Ling Ling Lv · Yong Cheng Wang · Hui Wen Liu · Qiang Wang

Received: 13 November 2009 / Accepted: 21 February 2010 / Published online: 10 March 2010

Abstract The activation mechanism of the nitrous oxide (N_2O) with the $Ta(NH_2)_3$ complex on the singlet and triplet potential energy surfaces has been investigated using the hybrid exchange correlation functional B3LYP. The minimum energy crossing point (MECP) is located by using the methods of Harvey et al. The rate-determining step of the N–O activation reaction is the intersystem crossing from ^{1}**2** to ^{3}**2**. The reacting system will change its spin multiplicities from the singlet state to the triplet state near MECP-1, which takes place with a spin crossing barrier of 32.5 kcal mol^{-1}, and then move on the triplet potential energy surface as the reaction proceeds. Analysis of spin–orbit coupling (SOC) using localized orbitals shows that MECP-1 will produce the significant SOC matrix element, the value of SOC is 272.46 cm^{-1}, due to the electron shift between two perpendicular π orbitals with the same rotation direction and the contribution from heavy atom Ta. The rate coefficients are calculated using Non-adiabatic Rice-Ramsperger-Kassel-Marcus (RRKM). Results indicate that the coefficients, *k(E)*, are exceedingly high, $k(E) > 10^{12}$ s^{-1}, for energies above the intersystem crossing barrier (32.5 kcal mol^{-1}); however, in the lower temperature range of 200–600 K, the intersystem crossing is very slow, $k(T) < 10^{-6}$ s^{-1}.

Keywords $Ta(NH_2)_3$ and N_2O · Spin–orbit coupling · Non-adiabatic RRKM

L. L. Lv · Y. C. Wang (✉) · H. W. Liu · Q. Wang
College of Chemistry and Chemical Engineering,
Northwest Normal University, 730070 LanZhou, Gansu, China
e-mail: lvling100@163.com

L. L. Lv
College of Life science and Chemistry,
Tianshui Normal University, 741001 Tianshui, Gansu, China

1 Introduction

Recently, there has been considerable concern about environmental issues associated with the growth of the N_2O concentration in atmosphere as a result of human activity [1], and in this global context, considerable efforts have been devoted to find ways of reducing anthropogenic emission of greenhouse nitrous oxide gas. Thus, the activation and cleavage of N_2O is one of the challenging subjects of academic research because they can provide fundamental information about catalytic bond activation. A large number of recent studies, both experimental and theoretical, have been devoted to the reactions of gas-phase transition metal atoms or ions with N_2O [2–14], which is well understood and studied.

However, the subject of small molecules activated processes via the three-coordinate ML_3 complex is still of considerable current interest since Laplaza and Cummins [15, 16] initially described the experimental cleavage of dinitrogen by a sterically hindered three-coordinate Mo(III) complex, $Mo[N(R)Ar]_3$(R = $C(CD_3)_2CH_3$, Ar = 3,5-$C_6H_3Me_2$) in 1995, resulting in the formation of a terminal nitride Mo(VI) product. More recent studies have shown that the class of sterically hindered three-coordinate metal complexes are extraordinarily versatile, capable of binding and activating a variety of small molecules, including N_2 [17, 18], SO_2 [19], CO [20], CN [21], CS_2 [22], NCO^- [23] and N_2O [24, 25]. The mechanistic details of the N_2O activation brought about by $Mo[N(R)Ar]_3$(R = $C(CD_3)_2CH_3$, Ar = 3,5-$C_6H_3Me_2$) have been computationally investigated using density functional theory (B3LYP) by Musaev and Morokuma [24]. The results show that the N–O bond activation is kinetically and thermodynamically more favorable. To predict which metals are most suitable for activating and cleaving small molecules such as N_2, NO

and CO, the M–L bond energies in the L–M(NH_2)$_3$(l = O, N, C) model complexes were calculated for a wide range of metals by Yates and coworkers [26]. Calculated results indicate that the thermodynamic driving force (M–L bond energies) for the activation of the small molecule is very strong in the L–Ta(NH_2)$_3$ (L = N and O) products. In other words, the N_2O activation by Ta(NH_2)$_3$ is thermodynamically more favorable.

But the chemistry of transition metals and their compounds is strongly influenced by the availability of multiple low-lying electronic states in these species [27–29]. This phenomenon particularly often occurs when the formal d-electron count on the metal is 2–8. This means that the reactions involve several electronic states that may also have different spins, should involve spin-conserving and spin-inversion processes [30]. The activation reaction of small molecules by M(NH_2)$_3$ could also occur intersystem crossing (ISC), such as activations of N_2 [17, 18] and N_2O [24, 25] by Mo(NH_2)$_3$, therefore, spin–orbit coupling (SOC) and intersystem crossing (ISC) rate play a key role in the activated processes. To our knowledge, these have been neglected during research processes. This is the motivation to investigate the title reaction. Therefore, a deep theoretical study for spin–orbit coupling (SOC) and intersystem crossing (ISC) rate is important in order to better understand the mechanism of the N_2O and Ta(NH_2)$_3$ reaction.

In the present article, we report a hybrid density functional theory (B3LYP) study of the reaction of the N_2O with Ta(NH_2)$_3$, as shown in Scheme 1. The minimum energy crossing point (MECP) between triplet and singlet PESs is identified by using the procedure of Harvey et al. [31], and possible spin-inversion processes and spin–orbit coupling (SOC) importance are deeply discussed in this intriguing chemical reaction. In addition, microcanonical rate coefficients $k(E)$ and canonical rate coefficients $k(T)$ for the spin-forbidden step from ^{1}2 to ^{3}2 are calculated using Non-adiabatic Rice-Ramsperger-Kassel-Marcus (RRKM) [32–34], which is compared to predicated rate coefficients for spin-forbidden dissociation of N_2O.

2 Computational details

2.1 Geometrical optimization

Computations were carried out using the Gaussian 03 ab initio program package [35] Energies and geometries of the reaction intermediates and the transition states were calculated with density functional theory (DFT) using the B3LYP level. The triple-zeta 6–311 + G(d) basis set of Pople and coworkers [36] was used for N, H and O, and the (8s7p6d) Stuttgart ECP [37] resulting in a (311111|31111|411)[6s5p3d] contraction was used for Ta. To further examine the relativistic effect of the choice of basis sets for Ta, the dissociation energies of the N–Ta(NH_2)$_3$ and O–Ta(NH_2)$_3$ bonds are calculated, they are 171.7 and 200.9 kcal/mol, respectively, by SDD basis set for Ta, which agree fairly well with the Yates' calculated values of 175.7 and 206.1 kcal/mol. Our calculation for Ta–N and Ta–O gave the bond distances of 1.831 and 1.750 Å, respectively, which are in good agreement with the Yates' calculated values of 1.804 and 1.737 Å. Previous investigations of transition metal compounds employing the B3LYP functional by other groups [38, 39] and us [40, 41] indicated that this approach shows a very

Scheme 1

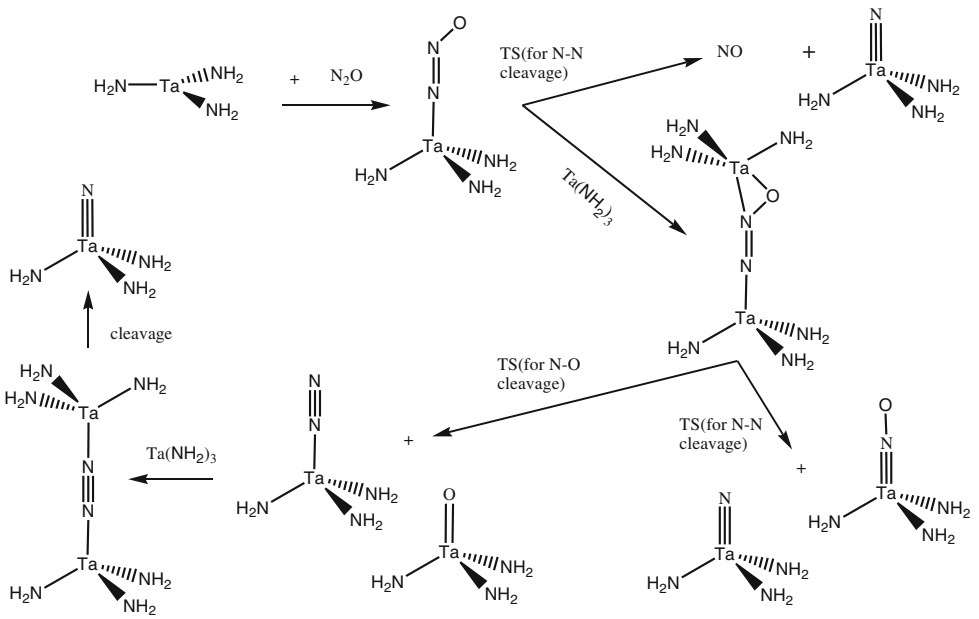

promising performance, to predict properties such as bond dissociation energies, geometries, harmonic frequencies and electronic details with an accuracy comparable to that obtained from highly correlated, wave function-based ab initio methods. Therefore, we are confident that the chosen B3LYP approach correctly describes the qualitative features of the PES.

All stationary points were characterized by vibrational analysis, and the zero-point energy (ZPE) was calculated. The transition state structures all represent saddle points, characterized by one negative eigenvalue of the Hessian matrix. The intrinsic reaction coordinate (IRC) was then calculated and used to track the minimum energy path from transition states to the corresponding minima, to probe the reaction path and check whether the correct transition state was located. The natural bond orbital (NBO) analyses were also carried out using the NBO 5.0 procedure [42]. The minimal energy crossing point (MECPs) between triplet and singlet PESs was identified by using the procedure of Harvey et al. [31] through a minimization procedure optimizing to a 50:50 mixture of singlet and triplet density matrices and gradients.

2.2 Spin–orbit coupling calculations

We estimated the SOC with the approximate one-electron spin–orbit Hamiltonian [43, 44] given in Eq. 1:

$$H_{\mathrm{SO}} = \frac{\alpha^2}{2}\sum_i \sum_A \left(\frac{Z_A^*}{r_{iA}^3}\right)(S_i \cdot L_{iA}) = \sum_i h_i(Z^*)\frac{\alpha^2}{2} = \frac{e^2 h}{4\pi m_e^2 c^2} \tag{1}$$

In which the neglect of the two-electron terms is compensated by introducing a semiempirical parameter. α is the fine structure constant, L_{iA} and S_i are the orbital and spin angular momentum operators for electron i in the framework of the nuclei indexed A, respectively, and Z_A^* is the effective nuclear charge.

The root-mean-squared value of the SOC constant is defined as Eq. 2.

$$SOC = \left(\sum_{M_S=\pm1,0}\sum_{k=x,y,z}\left\langle {}^3\Psi^{(M_S)}\middle|\hat{H}_{SO}\middle|{}^1\Psi\right\rangle_k^2\right)^{1/2} \tag{2}$$

The SOC constant is relevant to the electronic factor of the rate of the intersystem crossing. The SOC matrix elements in Eq. 2 were evaluated by using the singlet/triplet state-averaged complete active space self-consistent field [CASSCF (10, 8)] (10 electrons in 8 orbitals) wave function with corresponding to the 6–311 + G(d) basis set was used for N, O and H, the SBKJC ECP basis set is used for Ta (in order to be consistent with the Zeff parameters were given by Koseki et al. [45, 46]). For the qualitative interpretation of non-zero SOC interaction, we also used Boys localized orbitals generated at the triplet ROHF level as orbitals from which CASCI wave functions are constructed. All SOC calculations were performed with the GAMESS program package [47].

2.3 Non-adiabatic rate coefficient

The spin-forbidden processes have been accounted for by means of a non-adiabatic version of the RRKM [32–34] theory. In such cases, the microcanonical rate coefficient $k(E)$ of a non-adiabatic unimolecular is computed as

$$k(E) = \frac{2}{h\rho(E)}\int_0^E dE_h \rho_{MECP}(E - E_h)p_{sh}(E_h) \tag{3}$$

where h is Planck's constant, $\rho(E)$ is the reactant density of rovibrational states at energy E, $\rho_{MECP}(E - E_h)$ is the density of rovibrational states for the degrees of freedom within the crossing seam at the MECP, E_h is the part of the available energy, which is in the coordinate orthogonal to the seam. The term $p_{sh}(E_h)$ is the surface-hopping probability for a passage over the seam of crossing of the PESs, at the speed corresponding to energy E_h.

The probability of hopping $p_{sh}(E_h)$ can be calculated from Landau-Zener theory [48, 49] as shown in Eq. (4):

$$p_{sh}(E_h) = (1 - P_{LZ})(1 + P_{LZ})$$

where

$$P_{LZ} = \exp\left(\frac{-2\pi H_{12}^2}{\eta\Delta F}\sqrt{\frac{\mu}{2(E_h - E_{MECP})}}\right). \tag{4}$$

In this equation, H_{12} is the coupling matrix element between the two PESs and is constant in the vicinity of the MECP. ΔF is the relative slope of the two surfaces at the crossing point. The reduced mass of the system as it moves along the hopping coordinate is μ, and E_{MECP} is the energy of the MECP relative to reactants. In the above formula, $p_{sh}(E_h)$ represents the surface-hopping probability calculated as $(1 + \mathrm{P_{LZ}})$ $(1 - \mathrm{P_{LZ}})$, in which $(1 - \mathrm{P_{LZ}})$ and $\mathrm{P}(1 - \mathrm{P_{LZ}})$ are, respectively, the probability of hopping on first passage and the probability of not hopping on first pass, then hopping on the second pass.

When E_h is smaller than E_{MECP}, another expression of the probability of hopping has been suggested that allows for tunneling [50], as shown in Eq. (5).

$$p_{\mathrm{sh}}^{\mathrm{tunnel}}(E - E_{MECP}) = 4\pi^2 H_{12}^2\left(\frac{2\mu}{\eta^2 F\Delta F}\right)^{2/3} Ai^2 \times \left[(E - E_{MECP})\left(\frac{2\mu\Delta F^2}{\eta^2 F^4}\right)^{1/3}\right] \tag{5}$$

In this expression, F is the average of the slopes on the two surfaces, Ai denotes the Airy function, and H_{12}, μ and E_{MECP} have the same meaning as in Eq. (4).

A canonical expression for the rate coefficient is a function of temperature, as shown in Eq. (6).

$$k(T) = \frac{1}{hQ_R(T)} \int_0^\infty N_{MECP}(E) e^{-E/k_B T} dE \quad (6)$$

where $N_{MECP}(E) = \int_0^E dE_h \rho_{MECP}(E - E_h) p_{sh}(E_h)$, where $Q_R(T)$ is the partition function for the reactants. $N_{MECP}(E)$ denotes the effective integrated density of states in the crossing seam between the two surfaces. All the kinetic calculations were carried out using the CCSD(T) electronic energies and the B3LYP geometries and vibrational frequencies, corresponding to basis set is described in Geometrical optimization.

3 Results and discussion

3.1 Initial complexes

The optimized geometries and energetic data in the singlet and triplet electronic states are depicted in Fig. 1 and Table 1, respectively, where the superscripts denote the spin multiplicities. The overall reaction profile, showing the relative energies of the reactants, intermediates and products for the reaction given in Scheme 1, is plotted in Fig. 2.

In accordance with our studies, the singlet state of $Ta(NH_2)_3(^1\mathbf{1})$ is calculated to be more stable than the triplet state, $^3\mathbf{1}$, by about 2.5 kcal mol^{-1}. For d^2 complexes, the excited triplet state ($^3\mathbf{1}$) has one electron in the degenerate d_{xz} or d_{yz} MO and, therefore, is subject to a Jahn–Teller distortion structures (see Fig. 1), while for $^1\mathbf{1}$, the double d electron occupies the non-bonding dz^2 orbital, and so the orientation of the ligands would not be expected to affect its energy significantly. Thus, the non-bonding dz^2 level favors a coplanar ligand orientation.

The first step of reaction is coordination of the N_2O molecule to the Ta center of $Ta(NH_2)_3$, producing $(N_2O)Ta(NH_2)_3$ four-coordinate complex. In general, the N_2O molecule can bind to Ta via either of its terminal atoms N or O. Our calculation shows that O-approach is energetically unfavorable and results in no local minimum. The N_2O in singlet ground state binds to Ta via terminal N atom coordination and gives $^1\mathbf{2}$ with an energy drop of 47.5 kcal mol^{-1}. $^1\mathbf{2}$, having a singlet state, is about 20.9 kcal mol^{-1} more stable than $^3\mathbf{2}$, having a triplet state. The barrier height for the $^1\mathbf{1} + N_2O \rightarrow {}^1\mathbf{2}$ reaction is calculated to be 0.7 kcal mol^{-1}, almost without barrier process. As can be seen from Fig. 1, the Ta–N distance in $^1\mathbf{2}$ is found to be about 0.0849 Å shorter than in $^3\mathbf{2}$, and the N–N bond is elongated by 0.088 Å, indicating that the Ta–N_2O bonding interaction in $^1\mathbf{2}$ is stronger than in $^3\mathbf{2}$. The Mulliken charge distribution calculated for $^1\mathbf{2}$ and $^3\mathbf{2}$ further supports the discussion here. It follows from Fig. 3 that the electron population of N_2O increases from 0.0 in the free N_2O molecule to −0.41 in $^1\mathbf{2}$ and −0.37 in $^3\mathbf{2}$, suggesting that charge transfer plays a crucial role in the Ta–N_2O bonding interaction. The reactions of gas-phase transition metal atoms or ions with N_2O also support the calculated results here.

3.2 Surface-crossing behavior

Since $Ta[NH_2]_3$ has a singlet spin ground state and N_2O a singlet state, the reaction begins on the singlet surface. To reach the triplet encounter complex $^3\mathbf{2}$, an intersystem crossing occurs at the minimum energy crossing point (MECP). The MECP-1 is identified by using the methods of Harvey et al. [31], and the GAMESS program package [47]. The structure of MECP-1 is showed in Fig. 1 at the B3LYP level of theory. MECP-1 has a C_s geometry, in which the O–N, N–N and Ta–N bond distances are 1.2321, 1.2365 and 1.9299 Å, respectively. The structure is very similar with $^3\mathbf{2}$, corresponding to a late crossing point. In this MECP-1 crossing region, the reacting system should change its spin multiplicities from the singlet state ($^1\mathbf{2}$) to the triplet state ($^3\mathbf{2}$) and then moves on the triplet potential energy surface as the reaction proceeds. Within the seam, the MECP-1 point is a minimum, the spin hopping is easily taken place because the Franck–Condon principle requires that it has the same both energies and geometries. This crossing point is the most important role in this reaction pathway because the molecular system should change its spin multiplicity from the singlet state to the triplet state near this crossing region, leading to an intersystem crossing barrier height being 20.9 kcal mol^{-1}.

3.3 Analysis of spin–orbit coupling (SOC) near MECP-1

A spin-forbidden transition requires an effect of spin–orbit coupling (SOC) that provides a major mechanism for intersystem crossing [51, 52]. SOC induces a spin-multiplicity mixing that allows the wave function to break spin symmetry, and the magnitude of the spin-multiplicity mixing increases in a small energy gap between high- and low-spin states. Therefore, we must inspect the orbital relationships that promote the SOC matrix elements.

Localized orbitals for the construction of the singlet and triplet CASCI wave functions to be used in the SOC evaluation have been generated in the MECP-1 region by the triplet ROHF calculation followed by the Boys

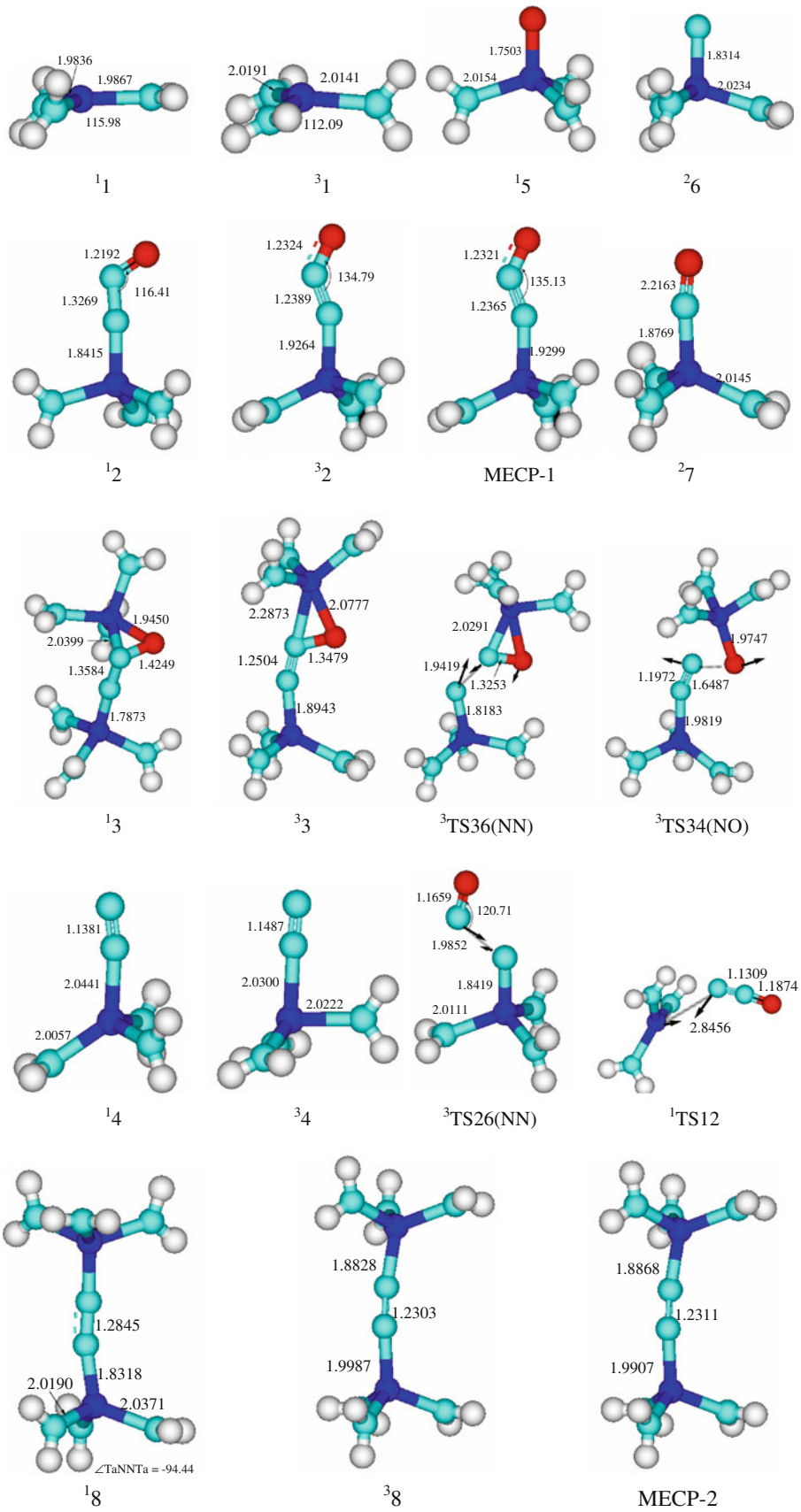

Fig. 1 Structures of several intermediates, MECP and transition states along the singlet and triplet surfaces of the $3Ta(NH_2)_3 + N_2O$ system calculated at the B3LYP level (bond lengths in angstroms and bond angles in deg). For each transition state, the transition vector corresponding to the imaginary frequency is shown

Table 1 Total energies E_{tot} (a.u.) and relative energies ΔE_{rel}(kcal/mol) for the optimized species are calculated at the B3LYP/6–311 + G(d) +SDD level

Species	State	The relation of molecular counts	ZPE	6–311 + G(d) + SDD	
				$E_{tot + ZPE}$	ΔE_{rel}
^{1}1 + N_2O	Cs, ^{1}A′ + $^1\Sigma$	3(^{1}1) + N_2O	0.08402	−859.44337	0.0
^{3}1 + N_2O	C_S, ^{3}A″ + $^1\Sigma$	3(^{3}1) + N_2O	0.08416	−859.43161	7.4
^{1}TS12	C_1, ^{1}A	^{1}TS12 + 2(^{1}1)	0.08545	−859.44225	0.7
^{1}2	C_1, ^{1}A	^{1}2 + 2(11)	0.08616	−859.51912	−47.5
MECP-1	C_S	MECP-1 + 2(^{1}1)	0.08616	−859.48574	−26.6
^{3}2	C_S, ^{3}A″	^{3}2 + 2(^{1}1)	0.08615	−859.48582	−26.6
^{3}TS26(NN)	C_1, ^{1}A	^{3}TS26(NN) + 2(^{1}1)	0.08379	−859.43309	6.5
^{1}3	C_1, ^{1}A	^{1}3 + ^{1}1	0.17539	−858.19581	782.7
^{3}3	C_S, ^{3}A″	^{3}3 + ^{1}1	0.16251	−859.60033	−98.5
^{3}TS36(NN)	C_1, ^{1}A	^{3}TS36(NN) + ^{1}1	0.16017	−859.53765	−59.2
^{2}6 + ^{2}7	Cs, ^{2}A′ + Cs, ^{2}A′	^{2}6 + ^{2}7 + ^{1}1	0.16094	−859.54128	−61.4
^{3}TS34(NO)	C_1, ^{1}A	^{3}TS34(NO) + ^{1}1	0.16077	−859.59484	−95.1
^{1}5 + ^{3}4	C_3, ^{1}A + C_S, ^{3}A″	^{1}5 + ^{3}4 + ^{1}1	0.16068	−859.68897	−154.1
^{1}5 + ^{1}4	C_3, ^{1}A + Cs, ^{1}A′	^{1}5 + ^{1}4 + ^{1}1	0.16159	−859.68010	−148.6
^{1}8	C_2, ^{1}A	^{1}8 + ^{1}5	0.16052	−859.81607	−233.9
MECP-2	C_1	MECP-2 + ^{1}5	0.16030	−859.74522	−189.4
^{3}8	C_1, ^{1}A	^{3}8 + ^{1}5	0.15915	−859.75061	−192.8
^{2}6	Cs, ^{2}A′	2(^{2}6) + ^{1}5	0.07835	−859.65975	−135.8

localization procedure [53]. At least four localized orbitals, as depicted in Fig. 4, are found to be essential to reproduce the qualitative trends of SOC in the ^{1}2 → ^{3}2 step; these are composed of two π type orbitals and two non-bonding orbitals, n_1 and n_2 (To certain extent delocalization). These localized orbitals form a basis for a subsequent SOCI. We have analyzed the origin of the non-zero SOC interaction by using the one-electron SOC operator, H_{SO1}. In ^{1}**2** → ^{3}**2** step, the triplet wave function of the MECP-1 using Boys localization orbitals can be satisfactorily expressed in Eq. 7, i.e. a single covalent configuration formally described as $^3\pi_1\pi_2$.

$$\left|{}^3\Psi^{(1)}\right\rangle = |n_1\bar{n}_1n_2\bar{n}_2\pi_1\pi_2\rangle \tag{7a}$$

$$\left|{}^3\Psi^{(0)}\right\rangle = 2^{-1/2}(|n_1\bar{n}_1n_2\bar{n}_2\bar{\pi}_1\pi_2\rangle + |n_1\bar{n}_1n_2\bar{n}_2\pi_1\bar{\pi}_2\rangle) \tag{7b}$$

$$\left|{}^3\Psi^{(-1)}\right\rangle = |n_1\bar{n}_1n_2\bar{n}_2\bar{\pi}_1\bar{\pi}_2\rangle \tag{7c}$$

On the other hand, the singlet wave function is given by the superposition of three covalent configurations and one Zwitterionic configuration (where the two electrons occupy the same orbitals), as shown in Eq. 8, in which $i = {}^1\pi_1\pi_2$, $^1n_2\pi_2$, $^1n_1\pi_2$ (see Fig. 7).

$$\left|{}^1\Psi\right\rangle = \sum_{i=1}^{3}\lambda_i\left|{}^1\Psi_{cov}(i)\right\rangle + \lambda_{ZW}|n_1\bar{n}_1n_2\bar{n}_2\pi_1\bar{\pi}_1\rangle \tag{8}$$

The $^1\pi_1\pi_1$ zwitterionic configuration wave function is the dominant configuration with the weight of about 0.9 at around the MECP-1 region. The permissible approximation of the triplet wave function by a single configuration enables us to analyze the SOC matrix element in a simple formula. Non-zero elements of the k-components ($k = x, y$, and z) of the SOC matrix, $\left\langle {}^3\Psi(M_S)\left|\hat{H}_{SO1}\right|{}^1\Psi\right\rangle_k$, are always proportional to the function, f_k, as given in Eq 9.

$$f_k = \lambda_{ZW}\langle\pi_1|\hat{h}_k|\pi_2\rangle - 2^{-1/2}\lambda_{n_2\pi_2}\langle n_2|\hat{h}_k|\pi_1\rangle - 2^{-1/2}\lambda_{n_1\pi_2}\langle n_1|\hat{h}_k|\pi_1\rangle \tag{9}$$

$$\left(\hat{h}_k = \frac{\alpha^2}{2}\sum_A\frac{Z_A\hat{l}_A^k}{r_A^3}\right)$$

where λ is the mixing coefficient, and Z_A is the nuclear charge. The most important aspect is the first term due to the two mutually perpendicular orbitals, and the $^1\pi_1\pi_1$ wave function is the dominant configuration with the weight of about 0.9. Therefore, to further understand the efficient SOC, it is very important that the SOC matrix element $\langle\pi_1|\hat{h}_k|\pi_2\rangle$ is discussed.

The MOs (π_1 and π_2) of the MECP-1 can be expressed as follows (Eq. 10):

$$\begin{aligned}\pi_1 &= c_{Ta}d_{Ta} + c_{N_2O}(p_N - p_N + p_O)\,\pi_2 \\ &= c'_{Ta}d'_{Ta} + c'_{N_2O}(p'_N - p'_N + p'_O)\end{aligned} \tag{10}$$

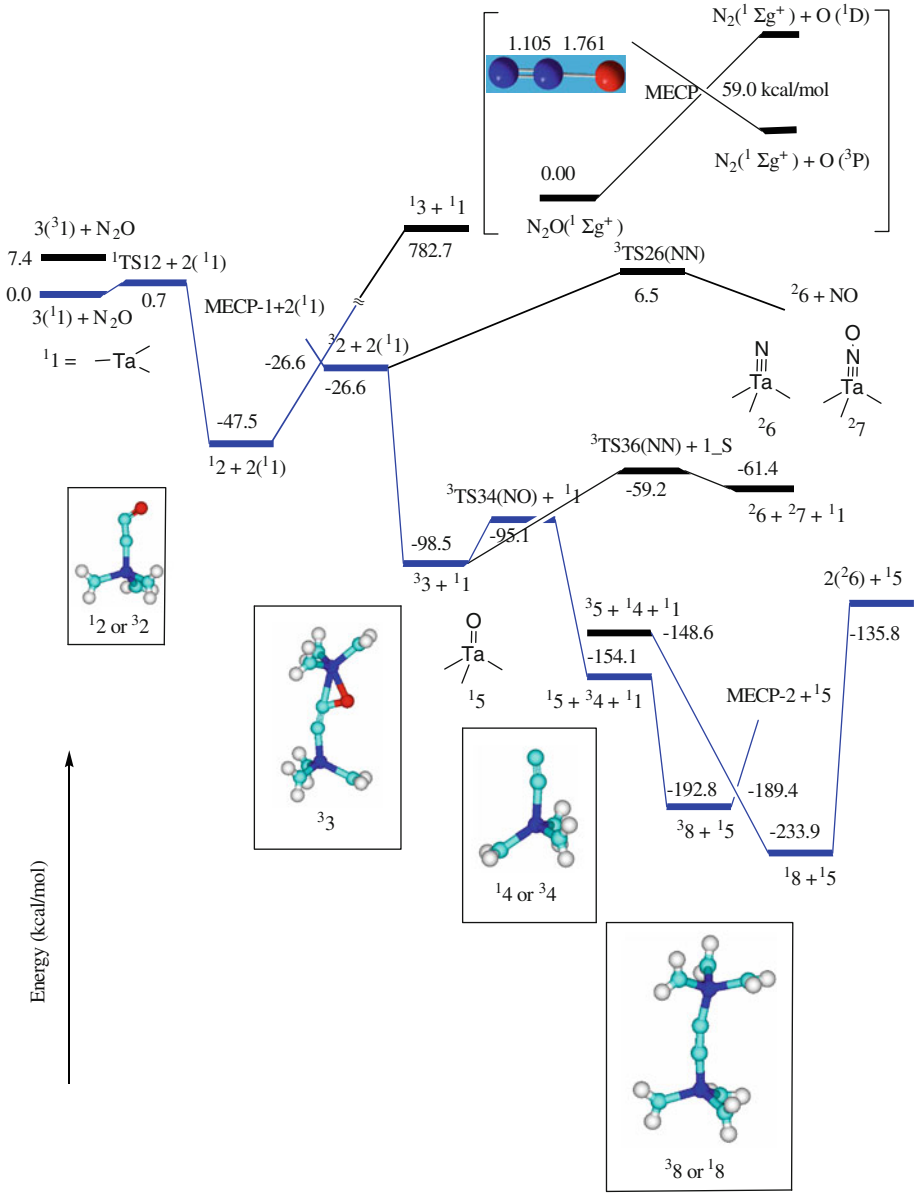

Fig. 2 Potential energy diagrams (include zero-point energy) for the reaction 3 $Ta(NH_2)_3 + N_2O$ in the singlet and triplet states. For comparing, that of N_2O is inserted in the *top* of diagrams. Relative energies are in kcal/mol. The potential energy surfaces provide a lower-energy pathway, which is indicated by the *blue line*

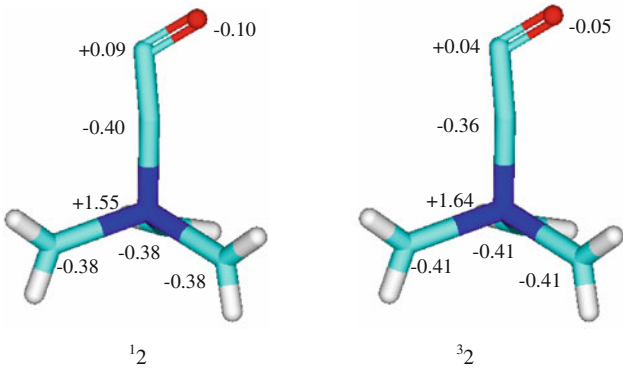

Fig. 3 Mulliken charges for species involved in the initial coordination of $Ta(NH_2)_3$ to N_2O

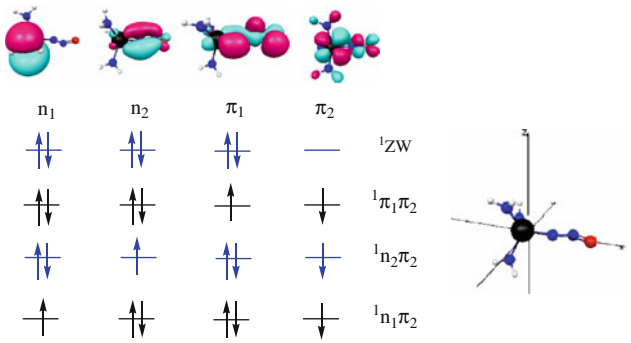

Fig. 4 Boys localized orbitals in the vicinity of the MECP crossing seam for the N–O bond activation step at the ROHF level and the orbital diagram of singlet covalent and Zwitterionic configurations

where the coefficients of the π_1 and π_2 orbitals are $c_{Ta}(c'_{Ta})$ and $c_{N_2O}(c'_{N_2O})$, respectively. Substituting Eq. 10 into Eq. 11, the x component of the SOC matrix element is given as

$$\langle SOC \rangle = 0.5 \sum_{I;J} C_I C_J \sum_k \langle \pi_1 | \hat{h}_k | \pi_2 \rangle \tag{11}$$

where we have already considered the non-vanishing spin factor (0.5), in the present case, the triplet configuration has one dominant coefficient, i.e. $C_I \approx 1$.

thus $\sum_J C_I C_J \approx \lambda_{ZW}$.

The final SOC expression becomes Eq. 12. Here, the m_d parameter is the coefficient of the angular momentum expectation values, while the cc' factors are products of the MO coefficients Eq. 10 for a given atom. The atomic constant terms, ζ, depend on the effective nuclear charge Z_A^* exerted on the valence electrons.

$$\langle SOC \rangle = 0.5 \lambda_{ZW} \left[m_d (c_{Ta} c'_{Ta}) \zeta_{Ta} + (c_{N_2O} c'_{N_2O}) \zeta_{N_2O} \right] (m_d = 1) \tag{12}$$

Equation 12 provides a basis for understanding the SOC matrix element. Obviously, N_2O term contribute to the SOC matrix element, but to a lesser extent than the Ta because ζ_{Ta} is far larger than ζ_{N2O}. Thus, to a rough approximation, the SOC matrix element will be determined by the variation of two main factors: the delocalization of the MOs as accounted for by the $c_{Ta}c'_{Ta}$ MO coefficient term and the ROHF configuration coefficient, C_J, of the singlet state. One can see from Fig. 7. From the π_1 orbital to the π_2 orbital, the MO coefficient, c'_{Ta} gets the bigger, and the singlet state dominated by a primary configuration ($C_J = 0.9$), such as MECP-1 possesses significant SOC matrix element, the value of SOC is 272.46 cm^{-1}, which is three times bigger than that of N_2O with the N–O dissociation crossing point (ca. 80 cm^{-1}). This can also be recognized from the UB3LYP spin density distribution at MECP-1, spin density mainly emerges on Ta, N (middle) and O atoms, the values of 0.79, 0.73 and 0.58, respectively (see Fig. 5). To confirm whether or not the qualitative trends obtained with the (6, 4) active space using Boys localized orbitals are valid, we have also evaluated SOC matrix elements by using MECP-1 state-averaged CASSCF (10, 8). The SOC value at MECP-1 of is calculated to be 267.3 cm^{-1}. The (6, 4) model based on localized orbitals will be adequate enough to analyze qualitatively the SOC patterns.

In addition, a non-zero angular momentum requires an electron to shift between two perpendicular AOs [43, 54, 55]. This shift creates an angular momentum along an axis that is perpendicular to the plane spanned by the AOs. An illustration is given in Fig. 7, where the two MOs are π_1 and π_2, and the electron shift from π_1 to π_2 creates an angular momentum in the x-direction. By the choice of the centers to be matched by the orbital rotation, here it is seen that the rotations are both in the same direction, as such MECP-1 will produce a significant one-center SOC interaction.

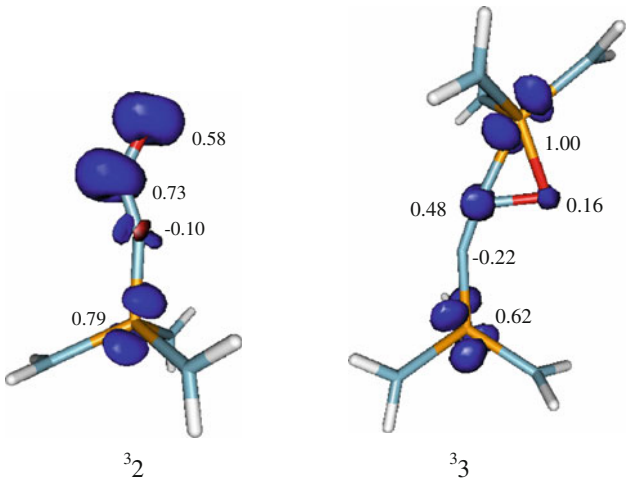

Fig. 5 Spin density changes during ^{3}2 → ^{3}3

3.4 Kinetics of the spin-forbidden ^{1}**2** → ^{3}2 step

We have characterized the minimum energy crossing point (MECP-1) connecting the singlet ^{1}**2** and triplet ^{3}**2**, whose optimized geometry is depicted Fig. 1. Microcanonical rate coefficients *k(E)* and canonical rate coefficients *k(T)* for the spin-forbidden ^{1}**2** → ^{3}2 step are calculated using non-adiabatic RRKM (see Fig. 6). To compute these reaction rates, the B3LYP/6–311 + G(d) + SDD harmonic frequencies and rotational constants were used, together with zero-point energy corrected relative energies from the CCSD(T)/6–311 + G(d) + SDD calculations. The slopes of the potential energy surfaces at MECP-1, required to compute $p_{sh}(E)$, are obtained directly from the B3LYP calculations. The assumption considers that the motion in the "hopping" direction, orthogonal to the seam, takes place independently of the "harmonic bath" motions, which are parallel to the seam. Thus, the reduced mass is calculated to be 10.3 amu.

As can clearly be seen in Fig. 6a, a trend is that the rate coefficients, *k(E)*, are exceedingly high for energies above the intersystem crossing barrier (32.5 kcal mol^{-1} at the CCSD(T) level, which provides an upper limit to the true barrier.). Below the barrier, the rates computed using the Landau-Zener expression (Eq. 4) is unable to account for the tunneling behavior, so that the rate coefficient is zero, but those given by Eq. 5 get more smaller down to low

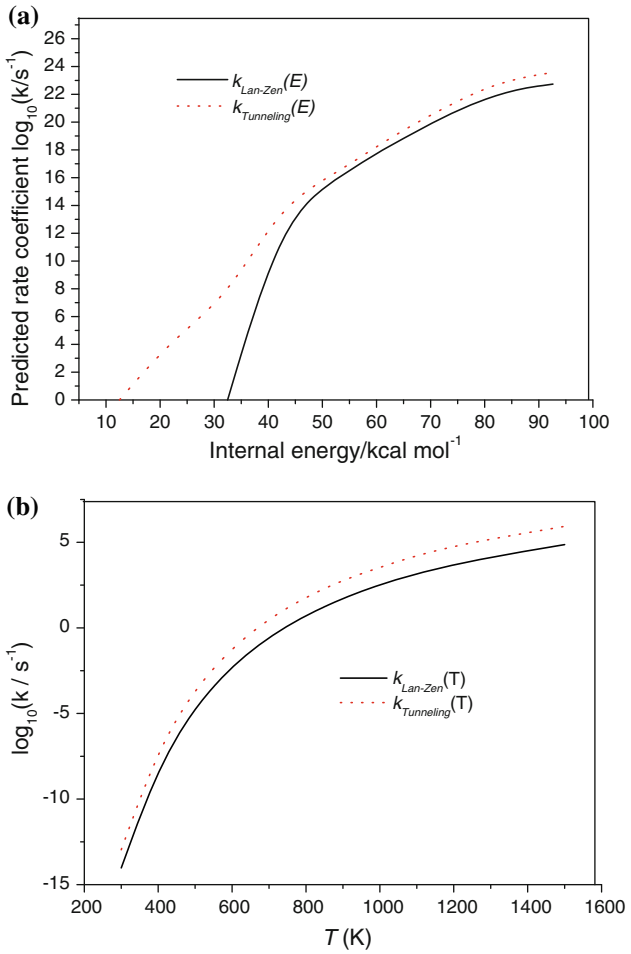

Fig. 6 Calculated microcanonical rate coefficients *k(E)*, and canonical rate coefficients *k(T)* for the spin-forbidden step from ^{1}2 to ^{3}2

energies. At the same time, the rate coefficient is predicted to be much larger than that of the N_2O spin-forbidden reaction (the N–O dissociation), *i.e.* the former, *k(E)*, is about 10^{16} s^{-1} at internal energy of 60 kcal mol^{-1}, while the latter is about 10^9 s^{-1}. From Fig. 6b, although there is significant SOC between the singlet and triplet states (the coupling matrix element is of 272.46 cm^{-1}), the reaction is still very much in the non-adiabatic regime, with a hopping probability of only about 0.047. These two factors of the barrier height and the spin-coupling contribute about equally to slowing this step. The rate constants show positive temperature dependence. At lower temperatures, 200–600 K, the spin-forbidden crossing is very slow, $k(T) < 10^{-6}$ s^{-1}, but changes of the *k(T)* values are very fast with temperature increased.

3.5 Mechanisms of ^{3}2 → products

After reaching the triplet state ^{3}**2**, as has been described earlier (Scheme 1), the activation of the N–N bond (mononuclear) and the formation of dinuclear intermediate with ^{3}**3** have a common intermediate, triplet state $(N_2O)Ta[NH_2]_3$, ^{3}**2**. The mononuclear mechanism proceeds further by a unimolecular N–N bond activation via the transition state, ^{3}**TS26(NN)**, producing one of the products, $NTa[NH_2]_3$, ^{2}**6**, and a molecule of nitric oxide NO. As seen in Fig. 1, the N–N cleavage transition state, ^{3}**TS26(NN)**, has only one imaginary frequency (234.41i cm^{-1}) corresponding to the N–N stretching reaction coordinate. In ^{3}**TS26(NN)**, the N–N bond distance is elongated significantly from 1.2389 Å in ^{3}**2** to 1.9852 Å. Meanwhile, the Ta–N bond shortens from 1.9264 Å in ^{3}**2** to 1.8419 Å. The N–O bond distance does not change significantly. All these geometrical differences between ^{3}**TS26(NN)** and reactant ^{3}**2** clearly indicate that this transition state indeed corresponds to formation of $NTa(NH_2)_3$, ^{2}**6**, and free NO molecule. The calculated barrier height of this process is 33.1 kcal mol^{-1} relative to ^{3}**2**.

Let us now compare the results between mononuclear and dinuclear mechanisms. The common intermediate for both mechanisms is the complex ^{3}**2**. In the mononuclear mechanism, ^{3}**2** will react unimolecularly over the ^{3}**TS26(NN)**, which has an activation free energy of 33.1 kcal mol^{-1}. On the other hand, in the binuclear mechanism, ^{3}**2** will react with the second $Ta(NH_2)_3$ to form a binuclear intermediate ^{3}**3**, which is calculated to be exothermic by 71.9 kcal mol^{-1} and is a barrierless process. As can be seen in Fig. 1, upon coordinate of the second $Ta(NH_2)_3$, the N–O bond is elongated by 0.116 Å, while the N–N bond do not change significantly. The results show that dinuclear mechanism is a favorable process.

From ^{3}**3**, the reaction splits into two paths, as seen in Scheme 1. The first of them is activation of the N–O bond. According to the results presented in Fig. 2, N–O bond activation in ^{3}**3** takes place quite easily via the transition state ^{3}**TS34(NO)**, with the barrier being only 4.4 kcal mol^{-1}. Structure ^{3}**TS34(NO)** is a real transition state with one imaginary frequency of 489i cm^{-1} corresponding to the N–O stretch (see Fig. 1). Going form ^{3}**3** to ^{3}**TS34(NO)**, the N–O bond is elongated from 1.3479 to 1.6487 Å. Obviously, from both structural and energetical points of view, the transition state ^{3}**TS34(NO)** is quite an early one. Overcoming this small barrier leads to formation of the products, $OTa(NH_2)_3$, ^{1}**5**, and $(N_2)Ta(NH_2)_3$, ^{3}**4**. This process is calculated to be exothermic by −154.1 kcal mol^{-1} relative to the reactants, 3(^{1}**1**) + N2O.

The second pathway originating at complex ^{3}**3** is the N–N activation through the transition state ^{3}**TS36(NN)**, leading to $NTa(NH_2)_3$, ^{2}**6**, and $(ON)Ta(NH_2)_3$, ^{2}**7**. The transition state ^{3}**TS36(NN)** has one imaginary frequency of 206i cm^{-1} corresponding to the N–N stretching. As seen from Fig. 1, the N–N bond is stretched from 1.2504 Å in ^{3}**3** to 1.9419 Å in ^{3}**TS36(NN)**. At the same time, two different Ta–N bonds shorten from 1.8943 and 2.2873 Å in ^{3}**3** to

1.8183 and 2.0291 Å in ^{3}**TS36(NN),** respectively. The calculated barrier height is 39.3 kcal mol^{-1} relative to structure ^{3}**3**.

Comparing the two different pathways starting from the complex ^{3}**3**, namely, N–O and N–N bond activation of the N_2O moiety, we conclude that (1) kinetically the N–O activation process, occurring with a 4.4 kcal mol^{-1} barrier, is much easier than N–N activation, which requires passing over a 39.3 kcal mol^{-1} barrier, and (2) the products ^{1}**5** and ^{3}**4** of the N–O bond activation process are thermodynamically more stable than the products ^{2}**6** and ^{2}**7** of N–N bond activation. Obviously, the dinuclear mechanism discussed earlier kinetically and thermodynamically favors N–O over N–N bond activation. In addition, the two-electron/two-orbital hyperconjugative interactions of electronic orbitals in space (stereoelectronic effects) are important for understanding molecular properties and chemical reactivity. Therefore, the more detailed information on the hyperconjugative interactions can be obtained by applying natural bond orbital (NBO) analysis [56]. The strengths of these interactions are estimated by second-order perturbation theory ($\Delta E^{(2)} = -2 < \sigma|\hat{E}|\sigma^* >/\varepsilon_{\sigma^*}-\varepsilon_{\sigma})$). It is found that the important interactions occur between the π(Ta–N) orbital(electron donor) and the empty σ^*(N–O) orbital, and between the σ(Ta–O) orbital and the σ^*(N–N) orbital in ^{3}**3**, as plotted in Fig. 7, corresponding to $\Delta E^{(2)}$, 12.6 and 3.4 kcal mol^{-1}, which shows that the transfer charges from π(Ta–N) to σ^*(N–O) are more stronger than that of both σ(Ta–O) and σ^*(N–N) orbitals, leading to the N–O bond cleaved easily. On the other hand, from Fig. 5, we also noted that the spin density of the O and N atoms is decreased, respectively, from 0.58 in ^{3}**2** to 0.16 in ^{3}**3,** and from 0.73 in ^{3}**2** to 0.48 in ^{3}**3**, while that of Ta (the second $Ta(NH_2)_3$) is increased from 0.0 in ^{1}**1** to 1.0 in ^{3}**3,** indicating that the spin density of N_2O has been shifted to the second $Ta(NH_2)_3$ through the O atom. In other words, the spin density on O is deplete due to the Ta–O bond formation while spin develops on the $OTa(NH_2)_3$ fragment that now possesses a singly occupied orbital to conserve the triplet character. These results discussed earlier indicate that the activation of the N–O bond in ^{3}**3** favors.

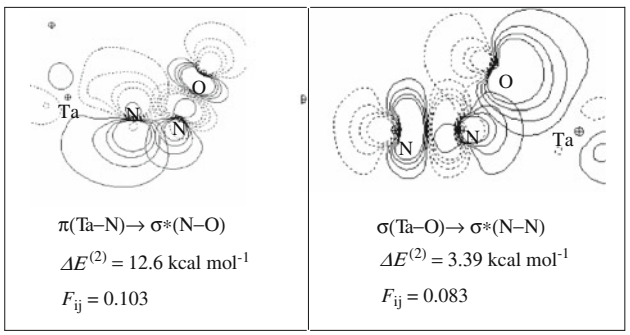

Fig. 7 Plots of two-dimension NBO interactions in the ^{3}3 from B3LYP/6–311 + G(d) +SDD

The next step of the reaction is expected to be coordination of the third fragment ^{1}**1** to ^{3}**4** (or ^{1}**4**). As can been seen from Fig. 2, once the cleavage process of the N–O bond has completed, the reaction further proceeds via coordination of $[NH_2]_3TaNN$ to a third $Ta[NH_2]_3$ complex, ^{1}**1**. The triplet complex ^{3}**8** is expected to be the product of the coordination reaction because the ground states for $[NH_2]_3TaNN$ and $Ta[NH_2]_3$ are triplet and singlet, respectively. The overall reaction $Ta[NH_2]_3 + {}^{3}\mathbf{4} \rightarrow {}^{3}\mathbf{8}$ is predicted to be strongly exothermic by 38.7 kcal mol^{-1} and has no barrier. Under C_{2h} and C_2 symmetry constrain conditions, the ^{3}**8** optimized appears imaginary frequencies. A spin crossover is required to form the singlet intermediate ^{1}**8**, which is 41.1 kcal mol^{-1} more stable than its triplet analog. To estimate the activation energy for the spin crossing process, the MECP-2 was identified by using the method of Harvey et al. [31] as mentioned previously (Fig. 1). The calculations show that the spin crossover occurs with a barrier of 3.4 kcal mol^{-1} at the B3LYP level of theory, and the value of spin–orbit coupling is 330.79 cm^{-1}. The result suggests that the formation of ^{1}**8** is a feasible process. Finally, we wish to point out that the conversion of ^{1}**8** to ^{2}**6** is thermodynamically unfavorable because it is a highly endothermic process.

4 Conclusions

The activation mechanism of the nitrous oxide(N_2O) with the $Ta(NH_2)_3$ complex on the singlet and triplet potential energy surfaces has been investigated at the density functional level of theory using the hybrid exchange correlation functional B3LYP. The minimum energy crossing point (MECP) is located by using the methods of Harvey et al. The first step of the reaction is the coordination of N_2O to the Ta center of $Ta(NH_2)_3$, leading to the formation of ^{1}**2**, (N_2O) $Ta(NH_2)_3$. The ^{1}**2** will change its spin multiplicities to the triplet state (^{3}**2**) via the minimum energy crossing point, MECP-1, and then moves on the triplet potential energy surface as the reaction proceeds. From ^{3}**2**, The mononuclear mechanism takes place via an N–N bond cleavage transition state and leads to the formation of $NTa(NH_2)_3$ and free nitric oxide NO. The dinuclear mechanism starts by the coordination of another Ta $(NH_2)_3$ to (N_2O)Ta $(NH_2)_3$, leading to the formation of $(NH_2)_3$Ta (N_2O) Ta $(NH_2)_3$, and splits further into two different paths, leading to N–O and N–N cleavage processes, among which the N–O activation is kinetically and thermodynamically more favorable. The rate-determining step of the N–O activation reaction is the intersystem crossing from ^{1}**2** to ^{3}**2**, which takes place with a spin crossing barrier of

32.51 kcal mol^{-1}. Analysis of spin–orbit coupling (SOC) indicates that there is the significant SOC matrix element (272.46 cm^{-1}) at MECP-1 due to the contribution of the heavy atom Ta. The rate coefficients are calculated using Non-adiabatic Rice-Ramsperger-Kassel-Marcus (RRKM). Results indicate that the coefficients, *k(E)*, are exceedingly high, $k(E) > 10^{12}$ s^{-1}, for energies above the intersystem crossing barrier (32.5 kcal mol^{-1}); however, in the lower temperature range of 200–600 K, the intersystem crossing is very slow, $k(T) < 10^{-6}$ s^{-1}.

Acknowledgment We wish to thank the National Natural Science Foundation of China (Grant No. 20873102) for the support of this research and we also thank TianShui Normal University for grant the 'QingLan' talent engineering funds.

References

1. Prather RA, Ehhalt DH (2001) In: Houghton JT et al (eds) Climate change 2001: the Scientific Basis. Cambridge University Press, New York
2. Tishchenko O, Vinckier C, Nguyen MT (2004) J Phys Chem. A 108:1268
3. Delabie A, Pierloot K (2002) J Phys Chem A 106:5679
4. Wiesenfeid JR, Yuen MJ (1976) Chem Phys Lett 42:293
5. Ritter D, Weisshaar JC (1989) J Phys Chem 93:1576
6. Ritter D, Weisshaar JC (1990) J Phys Chem 94:4907
7. Narayan SA, Futerko PM, Fontijn A (1992) J Phys Chem 96:290
8. Futerko PM, Fontijn A (1993) J Chem Phys 98:7004
9. Campbell ML, MeClean RE (1993) J Phys Chem 97:7942
10. Campbell ML (1996) J Phys Chem 100:19430
11. Stirling A (1998) J Phys Chem A 102:6565
12. Delabie A, Vinckier C, Flock M, Pierloot K (2001) J Phys Chem A 105:5479
13. Lv LL, Liu XW, Wang YC (2006) J Mol Struct: THEOCHEM 774:59
14. Lv LL, Liu XW, Wang YC (2005) J Mol Struct: THEOCHEM 724:185
15. Laplaza CE, Cumming CC (1995) Science 268:861
16. Laplaza CE, Odom AL, Davis WM, Cummings CC, Protasiewicz JD (1995) J Am Soc Chem 117:4999
17. Mindiola DJ, Meyer K, Cherry JPF, Baker TA, Cummins CC (2000) Organometallics 19:1622
18. Graham DC, Beran GJO, Head-Gordon M, Christian G, Stranger R, Yates BF (2005) J Phys Chem A 109:6762
19. Johnson AR, Davis WM, Cummins CC, Serron S, Nolan SP, Musaev DG, Morokuma K (1998) J Am Soc Chem 120:2071
20. Greco JB, Peter JC, Baker TA, Davis WM, Cummins CC, Wu G (2001) J Am Soc Chem 123:5003
21. Peters JC, Baraldo LM, Baker TA, Johnson AR, Cummins CC (1999) J Organomet Chem 591:24
22. Ariafard A, Brookes NJ, Stranger R, Yates BF (2008) J Am Soc Chem 130:11928
23. Fickes MG, Odom AL, Cummins CC (1997) Chem Commun No 20:1993
24. Khoroshun DV, Musaev DG, Morokuma K (1999) Organometallics 18:5653
25. Cherry JPF, Johnson AR, Baraldo LM, Tsai YC, Cummins CC, Kryatov SV, Rybak-Akimova EV, Capps KB, Hoff CD, Haar CM, Nolan SP (2001) J Am Soc Chem 123:7271
26. Christian GJ, Stranger R, Yates BF (2006) Inorg Chem 45:6951
27. Heinemann C, Cornehl HH, Schrolder D, Dolg M, Schwarz H (1996) Inorg Chem 35:2463
28. Armentrout PB (1991) Science 251:175
29. Rue C, Armentrout PB, Kretzschmar I, Schröder D, Harvey JN, Schwarz H (1999) J Chem Phys 110:7858
30. Yoshizawa K, Shiota Y, Yamabe T (1999) J Chem Phys 111:538
31. Harvey JN, Aschi M, Schwarz H, Koch W (1998) Theor Chem Accts 99:95
32. Harvey JN (2007) Phys Chem Chem Phys 9:331
33. Harvey JN, Aschi M (1999) Phys Chem Chem Phys 1:5555
34. Harvey JN, Aschi M (2003) Faraday Discuss 124:129
35. Frisch MJ et al (2003) Gaussian 03 (Revision-E.01). Gaussian Inc, Pittsburgh PA
36. Frisch MJ, Pople JA, Binkley JS (1984) J Chem Phys 80:3265
37. Dolg M, Stoll H, Preuss H (1989) J Chem Phys 90:1730
38. Cho HG, Andrew L (2006) J Phys Chem A 110:3886
39. Straub BF (2002) J Am Chem Soc 124:14195
40. Wang YC, Zhang JH, Geng ZY (2007) Chem Phys Lett 446:8
41. Wang YC, Wang Q, Geng ZY, Lv LL, Si YB, Wang QY, Liu HW, Cui DD (2009) J Phys Chem A 113:13808
42. Glendening ED, Badenhoop JK, Reed AE, Carpenter JE, Bohmann JA, Morales CM, Weinhold F (2001) NBO 5.0, Theoretical chemistry institute. University of Wisconsin, Madison
43. Danovich D, Marian CM, Neuheuser T, Peyerimhoff SD, Shaik S (1998) J Phys Chem A 102:5923
44. Isobe H, Yamanaka S, Kuramitsu S, Yamaguchi K (2008) J Am Chem Soc 130:132
45. Koseki S, Schmidt MW, Gordon MS (1998) J Phys Chem. A 102:10430
46. Koseki S, Fedorov DG, Schmidt MW, Gordon MS (2001) J Phys Chem. A 105:8262
47. Schmidt MW, Baldridge KK, Boatz JA et al (1993) J Comput Chem 14:1347
48. Zener C, Proc R (1932) Soc London Ser A 137:696
49. Zener C, Proc R (1933) Soc London Ser A 140:660
50. Delos JB (1973) J Chem Phys 59:2365
51. Lower SK, El-Sayed MA (1966) Chem Rev 66:199
52. Richards WG, Trivedi HP, Cooper DL (1981) Spin-orbit Coupling in Molecules. Oxford University Press, New York
53. Foster J, Boys SF (1960) Rev Mod Phys 32:300
54. Salem L, Rowland C (1972) Angew Chem Int Ed Engl 11:92
55. Michl J (1996) J Am Chem Soc 118:3568
56. Reed AE, Curtiss LA, Weinhold F (1988) Chem Rev 88:899